$Bi_2W_2O_9$: A potentially antiferroelectric Aurivillius phase

Hania Djani,[1,2] Emma E. McCabe,[3] W. Zhang,[4] P. S. Halasyamani,[4] A. Feteira,[5] Jordan Bieder,[2] Eric Bousquet,[2] and Philippe Ghosez[2]

[1]*Centre de Développement des Technologies Avancées, Cité 20 août 1956, Baba Hassen, Alger, Algeria*
[2]*Theoretical Materials Physics, Q-MAT, CESAM, Université de Liège, Allée 6 août, 17, B-4000, Sart Tilman, Belgium*
[3]*School of Physical Sciences, University of Kent, Canterbury, Kent CT2 7NH, United Kingdom*
[4]*Department of Chemistry, University of Houston, 112 Fleming Building, Houston, Texas 77204-5003, USA*
[5]*Department of Engineering and Mathematics, Sheffield Hallam University, Sheffield S1 1WB, United Kingdom*

(Received 3 March 2020; accepted 8 April 2020; published 29 April 2020)

Ferroelectric tungsten-based Aurivillius oxides are naturally stable superlattice structures, in which *A*-site deficient perovskite blocks $[W_nO_{3n+1}]^{-2}$ ($n = 1, 2, 3, \ldots$) interleave with fluorite-like bismuth oxide layers $[Bi_2O_2]^{+2}$ along the *c*-axis. In the $n = 2$ $Bi_2W_2O_9$ phase, an in-plane antipolar distortion dominates but there has been controversy as to the ground-state symmetry. Here we show, using a combination of first-principles density functional theory calculations and experiments, that the ground state is a nonpolar phase of *Pnab* symmetry. We explore the energetics of metastable phases and the potential for antiferroelectricity in this $n = 2$ Aurivillius phase.

DOI: 10.1103/PhysRevB.101.134113

I. INTRODUCTION

Ferroelectric oxides with naturally layered perovskite-like structures are a subject of intensive research due to their technological importance and to the interplay between competing structural instabilities that can give rise to complex phase transition scenarios [1]. Aurivillius compounds constitute a family of such layered perovskite-related materials in which fluorite-like $[Bi_2O_2]^{+2}$ layers alternate along the [001] stacking direction with perovskite $[A_{n-1}B_nO_{3n+1}]^{-2}$ blocks, with *n* being the number of layers of BO_6 octahedra in the perovskite block. Related families of layered perovskite-related materials include the Dion-Jacobson (DJ; of the general formula $A'A_{n-1}B_nO_{3n+1}$) and Ruddlesden-Popper families (RP; of the general formula $A_{n+1}B_nO_{3n+1}$). The RP and DJ phases have gained significant interest of late due to the appearance of noncentrosymmetric polar structures driven by the coupling of nonpolar structural distortions (including rotations of BO_6 octahedra) [2,3]. In contrast, the Aurivillius phases have been known for some time as "proper" ferroelectrics in which the primary order parameter describes in-plane polar displacements [4,5].

The Aurivillius series $Bi_2W_nO_{3n+3}$ consists of structures composed of perovskite blocks of corner-linked WO_6 octahedra *n* layers thick, with no *A* cations in these perovskite blocks (i.e., layered analogs to WO_3). These perovskite blocks are separated by fluorite-like bismuth oxide layers. Their ideal or aristotype structures are of tetragonal $I4/mmm$ symmetry, but as for other Aurivillius phases, numerous structural distortions (including tilts of WO_6 octahedra and cation displacements) are possible.

The $n = 1$ member of the series, Bi_2WO_6, the mineral known as russellite, is ferroelectric at room temperature, adopting a polar crystal structure of $P2_1ab$ symmetry with in-plane polar displacements and octahedral tilts around both in-plane and out-of-plane axes [6–10].

The $n = 2$ member of the series, $Bi_2W_2O_9$, was first reported in 1938 [11]. Its structure was investigated by Bando *et al.* in 1979 using electron diffraction analysis and high-resolution electron microscopy. It was described in terms of in-plane antipolar displacement of cations and octahedral tilts about both in-plane and out-of-plane axes. Although a polar space group ($Pna2_1$) was assigned, $Bi_2W_2O_9$ was described as potentially antiferroelectric, with in-plane cation displacements that are antiparallel from layer to layer along the [001] direction [12]. This model of $Pna2_1$ symmetry also implies an out-of-plane polar displacement along [001] which is rarely observed in Aurivillius phases but has been accepted as the ground-state structure of $Bi_2W_2O_9$ on the basis of x-ray diffraction studies [11].

Antiferroelectrics (AFEs) form a class of functional materials that adopt a nonpolar ground state but can undergo a phase transition in an applied electric field to a polar ferroelectric state, provided that the nonpolar and the polar phases are close enough in energy [13]. Such a field-induced phase transition gives rise to peculiar double hysteresis *P* versus *E* loops, which are appealing for data storage applications. Given the scarcity of antiferroelectric materials, the suggestion that $Bi_2W_2O_9$ might be antiferroelectric warrants further investigations.

Here, we report first-principles density functional theory (DFT) calculations and symmetry analysis to explore theoretically the Born-Oppenheimer energy landscape of $Bi_2W_2O_9$ as well as neutron powder diffraction (NPD), second-harmonic generation (SHG), and dielectric polarization measurements to support the assignment of the ground state. Our study shows that $Bi_2W_2O_9$ adopts a nonpolar ground state of *Pnab* symmetry (as illustrated in Fig. 1) involving only antipolar displacements and in-plane and out-of-plane octahedral tilts. DFT calculations reveal the presence of a metastable polar phase of $A2_1am$ symmetry (a common ground state of $n = 2$

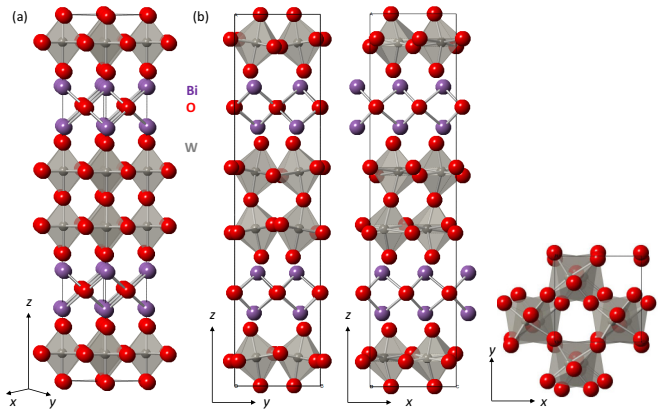

FIG. 1. The structure of $Bi_2W_2O_9$ in (a) the aristotype paraelectric $I4/mmm$ phase and (b) the distorted orthorhombic $Pnab$ ground state showing rotation of WO_6 octahedra about in-plane and out-of-plane axes and in-plane antipolar displacements of W^{6+} ions. Bi, W, and O ions are shown in purple, gray, and red, respectively, and corner-linked WO_6 octahedra are shown in gray.

Aurivillius phases [8,14]) only slightly higher in energy than the nonpolar ground state. This metastable polar phase is consistent with AFE behavior, which unfortunately could not be accessed experimentally.

II. METHODS

A. First-principles calculations

Calculations were performed within DFT [16,17] using a plane-wave method thanks to the ABINIT package [18–20]. The exchange correlation energy functional was evaluated within GGA PBEsol [21], and Bi ($5d$, $6s$, $6p$), W ($5s$, $5p$, $5d$, $6s$), and O ($2s$, $2p$) levels were treated as valence states in the norm-conserving pseudopotentials as delivered from the pseudodojo project [22]. The wave functions were expanded up to a kinetic energy cutoff of 50 Hartrees. Integrals over the Brillouin zone were approximated by sums on a $6 \times 6 \times 1$ Monkhorst-Pack mesh of special k-points [23]. The structural optimization was done using the Broyden-Fletcher-Goldfarb-Shanno minimization algorithm (BFGS) [24]. We calculated the *ab initio* forces on the ions and relaxed the position of each atom until the absolute value of forces converged to less than 10^{-5} Ha/Bohr. Phonons were calculated using density functional perturbation theory [25,26] and spontaneous polarization using the Berry phase formalism [27].

B. Synthesis

A polycrystalline sample of $Bi_2W_2O_9$ was prepared as a pale yellow powder by solid-state reaction. Stoichiometric quantities of Bi_2O_3 (Alfa Aesar, 99.99% purity) and WO_3 (Sigma Aldrich, 99% purity) were ground together in an agate pestle and mortar and reacted in air at 750 °C for 12 h and at 800 °C for 36 h with intermittent grinding.

C. Characterization

Powder x-ray (XRPD) data were collected at room temperature using a PANalytical X'Pert3 powder diffractometer using Cu $K\alpha_1$ radiation, an X'Celerator detector, and step size 0.04°. Low-temperature XRPD data were collected using an Oxford Cryosystems Phenix cryostat with the sample sprinkled onto a zero-background silicon wafer, and ∼40 min scans were collected upon warming from 12 K to room temperature. Neutron powder diffraction (NPD) data were collected on the HRPD diffractometer (ISIS Neutron and Muon Source). An ∼8 g sample was loaded into a cylindrical vanadium can, and data were collected at room temperature over 4 h using both a 30–130 ms window and a longer d-spacing 100–200 ms window. Diffraction data were analyzed using the Rietveld method [28] using TOPASACADEMIC software [29]. Combined x-ray and neutron (three data banks) refinements were carried out, primarily using the 30–130 ms NPD window. The background (shifted Chebyshev), zero point or sample height (DIFA/DIFC for neutron refinements), peak profiles, lattice parameters, atomic positions, and isotropic thermal parameters were refined. Preferred orientation (using a March-Dollase function with a single preferred-orientation direction, consistent with a platelike morphology for this top-loaded and pressed sample) was included to fit the XRPD data [30,31]. To check sample stoichiometry, the *Pnab* model with a single global temperature factor was used for combined Rietveld refinement to refine fractional occupancies of Bi and O sites (while the W site occupancy was fixed at unity). This suggested occupancies close to unity for all sites [0.9886(7), 1.005(1), 0.997(3), 0.972(2), 0.978(2), and 0.987(2) for Bi, O(1), O(2), O(3), O(4), and O(5) sites, respectively], consistent with a composition close to stoichiometric. The web-based ISODISTORT software [32] was used to explore possible structural distortions in terms of symmetry-adapted distortion modes.

$Bi_2W_2O_9$ was tested for a second-harmonic-generation (SHG) signal using the experimental setup described in Ref. [33]; a $Bi_2W_2O_9$ pellet was ground and sieved into distinct particle size ranges (<20, 20–45, 45–63, 63–75, 75–90, and 90–125 μm). Relevant comparisons with known SHG materials were made by grinding and sieving crystalline KH_2PO_4 (KDP) into the same particle size ranges. SHG intensity was recorded for different particle size ranges. No index matching fluid was used in any of the experiments.

Dielectric polarization measurements were carried out on sintered pellets of $Bi_2W_2O_9$: single-phase $Bi_2W_2O_9$ powders were pressed under a uniaxial applied load of 1 ton using a steel die with a diameter of 10 mm (Specac). These green bodies were subsequently fired in air at 860 °C for 2 h to give dense ceramics suitable for high electric field measurements. Gold-sputtered electrodes were applied onto both faces of the fired ceramics, and field-induced measurements were performed between −100 and 140 °C using an aixACCT system. Polarization (P) versus electric field (E) loops and leakage currents were recorded using a triangular signal at a frequency of 1 Hz. In addition, the P versus E response of ferroelectric Bi_2WO_6 ceramics was also measured for comparison.

III. RESULTS

A. First-principles calculations

As mentioned in the Introduction, the high-symmetry reference structure of Aurivillius compounds is of $I4/mmm$

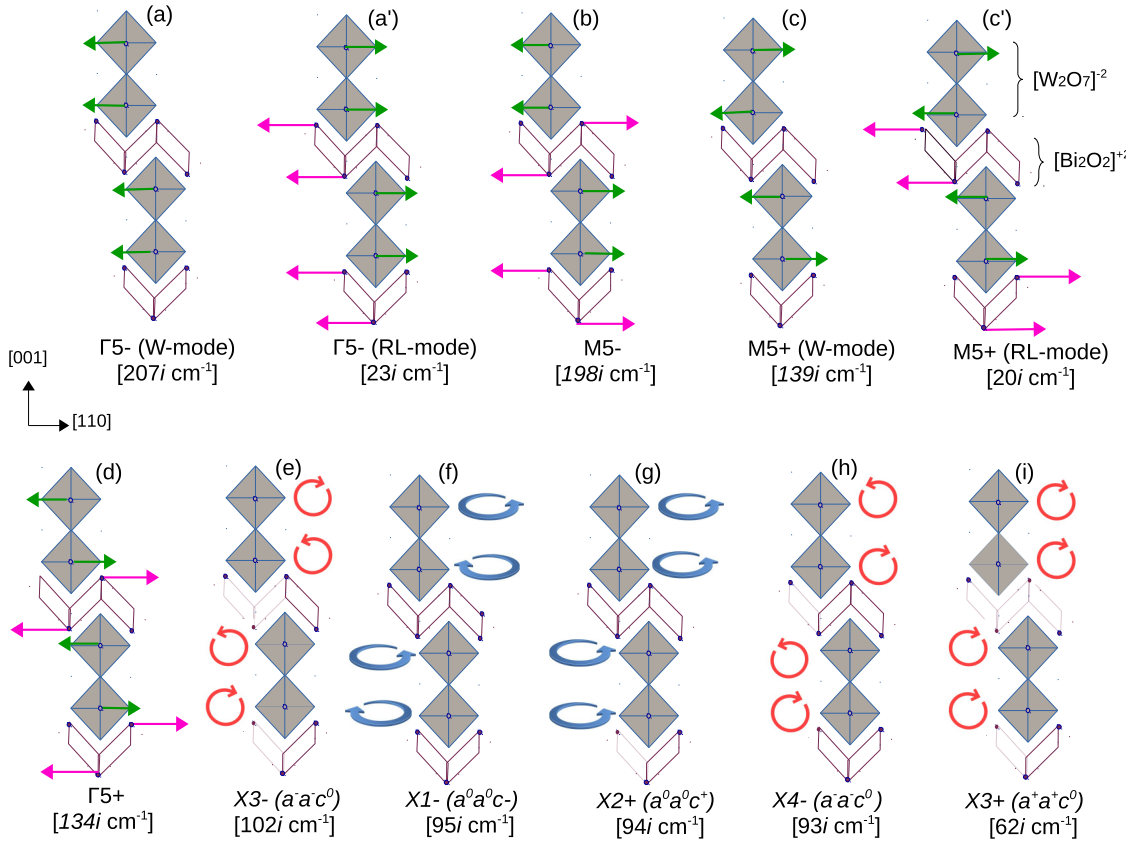

FIG. 2. Schematic illustration of atomic motions associated with the unstable phonon modes of the $I4/mmm$ phase of $Bi_2W_2O_9$ (at high-symmetry points of the Brillouin zone). Rigid-layer modes (RL modes) are related to a nearly rigid motion of the $[Bi_2O_2]^{+2}$ layer with respect to the perovskite block [6,15]. For modes involving polar and antipolar cationic displacements, oxygen atom motions are omitted for clarity. The [110] direction is that in the tetragonal primitive cell and corresponds to the a-axis in the orthorhombic cell.

symmetry. To explore which combination of distortions can lower the energy and produce the ground state, phonon calculations are performed in the $I4/mmm$ paraelectric phase of $Bi_2W_2O_9$. Numerous phonon instabilities are identified at high-symmetry points, as illustrated in Fig. 2. They include, on the one hand, in-plane atomic motions such as (a)–(a′)Γ_5^- polar motions [W and rigid-layer (RL) modes], (b) M_5^- interblock antipolar motions, (c)–(c′) M_5^+ intrablock antipolar motions (W and RL modes), and (d) Γ_5^+ intrablock antipolar motions and, on the other hand, rotations of WO_6 octahedra about [001] and [110] axes, such as (e) X_3^- rotation pattern $a_t^-a_t^-c^0/a_t^-a_t^-c^0$, (f) X_1^- rotation pattern $a_t^0a_t^0c^-/a_t^0a_t^0c^-$, (g) X_2^+ rotation pattern $a_t^0a_t^0c^+/a_t^0a_t^0c^+$, (h) X_4^- rotation pattern $a_t^-a_t^-c^0/-(a_t^-a_t^-c^0)$, and (i) X_3^+ rotation pattern $a_t^+a_t^+c^0/a_t^+a_t^+c^0$ (with t referring to the primitive tetragonal cell).

Condensation of these various instabilities (individually or together) into the reference $I4/mmm$ model, followed by full relaxation of atomic coordinates and cell parameters, allows one to identify a set of lower-energy (quantified by a negative ΔE) metastable phases, as summarized in Fig. 3.

Considering first the metastable phases resulting from the condensation of individual unstable modes, the largest energy lowerings result from the M_5^+ mode consisting of antipolar motions within the perovskite block ($Cmca$ phase), followed by the polar Γ_5^- displacement ($Fmm2$ phase). The antipolar modes M_5^- ($Cmcm$ phase) (consisting of antipolar motion between perovskite blocks) and $\Gamma5^+$ ($C2/m$ phase) yield smaller but still sizable energy lowerings. By contrast, distortions involving octahedral tilts produce significantly smaller energy lowerings with, in decreasing order, X_3^- ($Amam$ phase, nonstandard setting of $Cmcm$), X_4^- ($Bbcb$ phase, nonstandard setting of $Cmma$), X_1^- ($Bbab$ phase, nonstandard setting of $Ccca$), X_2^+ ($Acam$ phase, nonstandard setting of $Cmca$), and X_3^+ ($Abam$ nonstandard setting of $Cmca$). This hierarchy corresponds to what is observed in WO_3, in which the polar and antipolar distortions lower the total energy much more than the octahedral tilts [34]. This is in contrast with other Aurivillius phases like Bi_2WO_6, in which octahedral tilts and polar distortions give comparable energy gains (although the tilts are much less unstable than the polar mode). In $SrBi_2Ta_2O_9$, the strongest instability is the octahedral tilt X_3^- mode, which gives a similar energy lowering to the less unstable polar mode [8].

Considering now the condensation of combinations of unstable modes, additional phases at lower energies can be identified. The most stable phases are those resulting from the condensation of M_5^+ or Γ_5^- displacements and $a^-a^-c^0$ (X_3^- or X_4^-) tilts (i.e., models of $Pnab$, $Pcaa$, or $A2_1am$ symmetry). As noted by Zhang *et al.* [35], the "sign" of rotation pattern around the in-plane axis from one perovskite block to the next [i.e., $a_t^-a_t^-c^0/+(a_t^-a_t^-c^0\ X_3^-)$ tilts, or $a_t^-a_t^-c^0/-(a_t^-a_t^-c^0)$ X_4^- tilts], changes the symmetry (and energy) of the resulting phase.

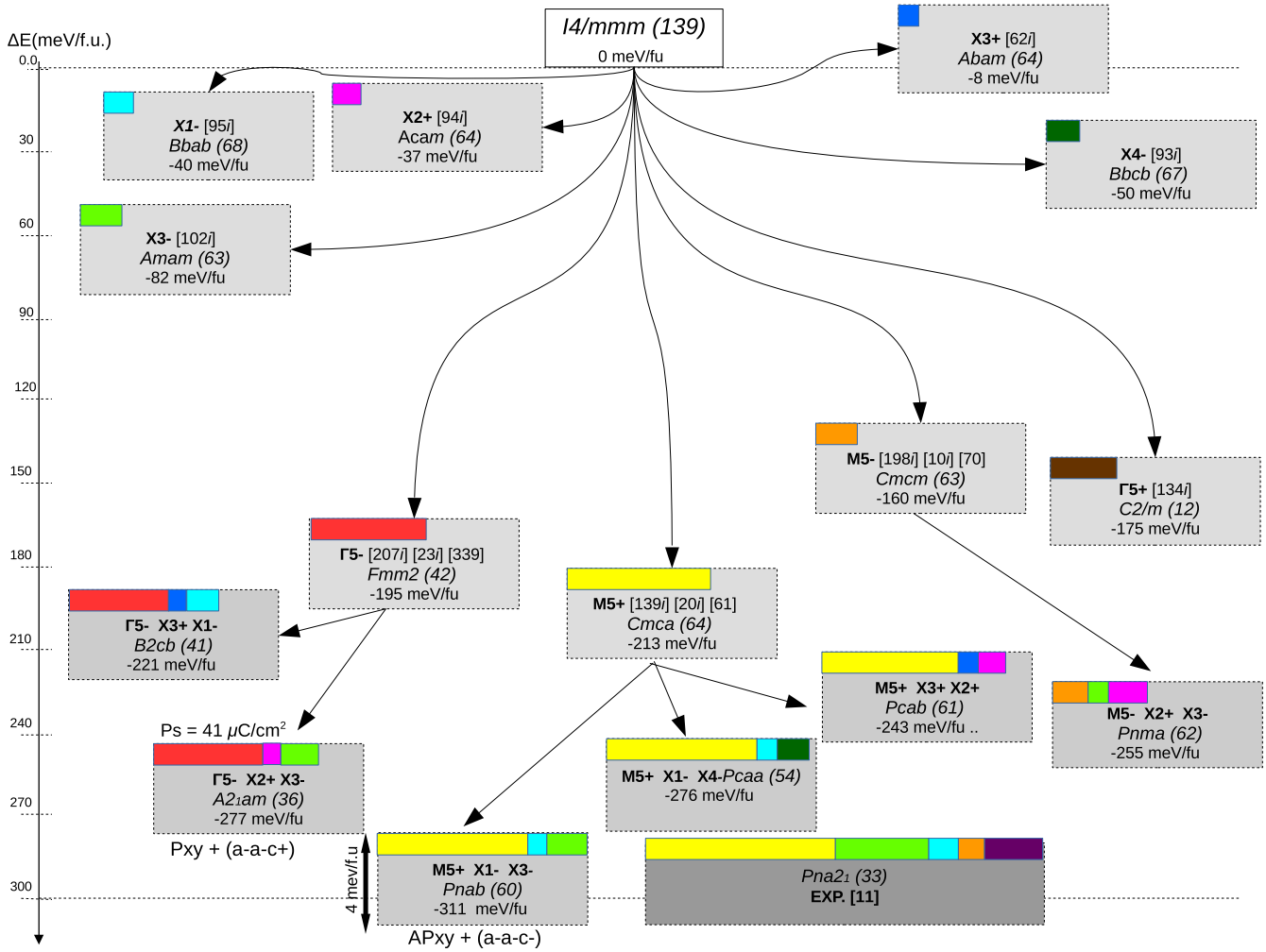

FIG. 3. Sketch of the most relevant metastable phases of $Bi_2W_2O_9$. Each phase is identified by the combination of modes giving rise to it, its symmetry, and its energy (ΔE in meV per formula unit) with respect to the $I4/mmm$ reference model. Contributions of the modes of a given symmetry to the total atomic distortion of each phase with respect to the $I4/mmm$ reference model are identified through color segments, with lengths proportional to the projection ($A\alpha_i$; see the main text) of these modes to the total distortion. A distinct color is affected to modes of distinct symmetry. When different modes of the same symmetry are contributing, only their total contribution is shown. The $Pna2_1$ phase from Ref. [11], although not a metastable phase in our computational framework, is included (darker gray box) for comparison.

The combination of one of the in-plane polar/antipolar displacements (Γ_5^-/M_5^+) with one of the in-plane axis tilts (X_3^-, X_4^-, and X_3^+) allows systematically the emergence of a second out-of-plane axis octahedral tilt (X_1^- or X_2^+ tilts) by trilinear coupling. This is in contrast to Bi_2WO_6, for which in-plane and out-of-plane axis octahedral tilts (X_3^+ and X_2^+ modes) combine with the polar Γ_5^- mode in the $P2_1ab$ ground state without the action of trilinear coupling [6].

To characterize the atomic distortion Δ of each metastable phase with respect to the $I4/mmm$ tetragonal reference structure, we can express Δ in the basis of atomic displacements formed by the phonon eigendisplacement vectors η_i of the $I4/mmm$ phase (such that $\langle \eta_i | M | \eta_j \rangle = \delta_{ij}$), following the scheme explained in Ref. [6]: $\Delta = A \sum_i \alpha_i \eta_i$, where A is the total distortion amplitude and α_i are the relative mode contributions such that $\sum_i \alpha_i^2 = 1$. The contributions of distinct phonon modes i to the distortion Δ of a given phase correspond, therefore, to the amplitudes $A\alpha_i$, illustrated in distinct colors in Fig. 3.

The condensation of an unstable mode of a given symmetry automatically allows the appearance of other unstable and stable modes of the same symmetry. In particular, the condensation of Γ_5^--W or M_5^+-W modes allows the related unstable RL-modes, as well as stable harder modes that have significant contributions to the total distortion. When different modes of the same symmetry appear together, only their global contribution is shown for simplicity in Fig. 3 [36] while detailed individual mode-by-mode contributions are reported in the supplemental material [37].

We have seen that the largest lowerings of energy are produced by the M_5^+ and Γ_5^- distortions, the *Cmca* phase being a little lower in energy than the $Fmm2$ phase. The additional condensation of X_3^- in both these phases then brings the system to the *Pnab* and $A2_1am$ phases with the appearance of a very similar third mode in each case (X_1^- or X_2^+). As shown in Fig. 3, the distortion amplitudes in the *Pnab* and $A2_1am$ phases remain very similar to those in the phases with single distortions, and the total energy lowerings

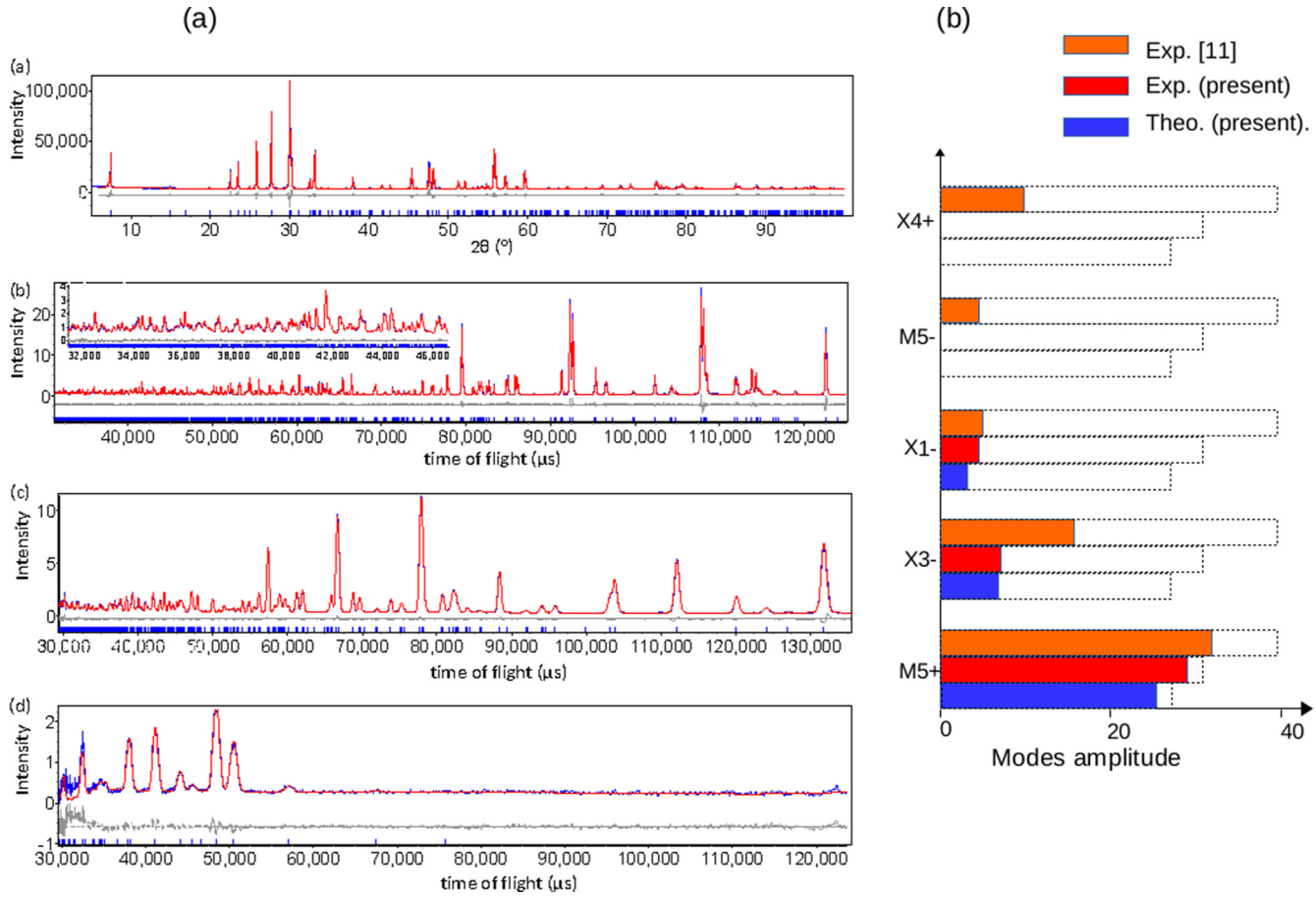

FIG. 4. (a) Rietveld refinement profiles from combined refinement using (a) XRPD data; (b) backscattered 169° bank data (∼0.6 − 2.6 Å d-spacing range), including an enlarged view of low d-spacing range; (c) 90° bank data (∼0.8 − 3.8 Å d-spacing range); and (d) 30° bank data (∼2.3 − 9 Å d-spacing range) collected for $Bi_2W_2O_9$ at room temperature using the *Pnab* model. Observed and calculated (upper) and difference profiles are shown by blue, red, and gray lines, respectively. (b) Decomposition of the full atomic distortion with respect to the $I4/mmm$ reference model for the $Pna2_1$ phase of Ref. [11] (orange), the present *Pnab* phase refined from our diffraction data (red), and the present *Pnab* phase relaxed from first-principles calculations. The dashed boxes show the total distortion amplitudes (A), while the color segments show the respective contributions ($A\alpha_i$) of the modes of distinct symmetry.

are roughly comparable to the sum of the energy lowerings produced by the individual distortions. This highlights that all these distortions are only weakly coupled (i.e., they do not strongly compete nor cooperate). So, the X_3^- distortion plays a very important role in further decreasing the energies of the $Fmm2$ and *Cmca* phases, but it does not revert their relative stability.

From this, we identify the *Pnab* phase, combining in-plane antipolar M_5^+ cation displacements, X_1^- out-of-plane axis octahedral rotation, and X_3^- in-plane axis octahedral tilt, as the ground-state structure of $Bi_2W_2O_9$. Allowing additional condensation of the Γ_3^- out-of-plane polar displacements does not provide any extra energy gain. It is noticeable that the $Pna2_1$ model reported in the literature [11,12,38] has similar contributions from M_5^+, X_3^-, and X_1^- distortions, but involves additional X_4^+ and M_5^- modes [see Fig. 4(b)]. These modes break the inversion symmetry, allowing the appearance of out-of-plane polar displacement Γ_3^- thanks to trilinear couplings: $M_5^+ \oplus M_5^- \oplus \Gamma_3^-$ and $X_3^- \oplus X_4^+ \oplus \Gamma_3^-$. A full structural relaxation of this literature model only preserves M_5^+, X_1^-, and X_3^- distortions and suppresses X_4^+ and M_5^-, consistent with the *Pnab* ground state. Further phonon calculations in *Pnab* show no remaining instability, ruling out the possibility of going from *Pnab* to $Pna2_1$ by adding either X_4^+, M_5^-, or Γ_3^-.

$Bi_2W_2O_9$ might have been expected to adopt a polar $A2_1am$ ground state, in line with other stoichiometric $n = 2$ Aurivillius phases. In $Bi_2W_2O_9$, such a polar phase is metastable and significantly stabilized with respect to the reference $I4/mmm$ phase, but it appears 34 meV/f.u. higher in energy than the *Pnab* ground state. From Berry phase calculations [39], the spontaneous polarization of $A2_1am$ phase is estimated to be 41 μC cm^{-2} [40] along the a-axis of the orthorhombic cell. Although $Bi_2W_2O_9$ is not ferroelectric, following Rabe [13], the proximity in energy of this $A2_1am$ polar phase with the nonpolar *Pnab* ground state makes it a potential antiferroelectric material. Indeed, by applying an electric field, it might be possible to stabilize the $A2_1am$ phase against the *Pnab* one and open a double hysteresis loop typical of an antiferroelectric. The field $\mathcal{E}_c$ required to make the $A2_1am$ phase thermodynamically more stable than the *Pnab* phase can be estimated by $\mathcal{E}_c = \Delta E/\Omega_0 P_s$, where ΔE is the energy difference between the two phases (34 meV/f.u.), P_s is the spontaneous polarization of the polar phase (41 μC cm^{-2}),

and Ω_0 is its unit-cell volume (690 Å), yielding the relatively modest value $\mathcal{E}_c = 192$ kV/cm.

B. Neutron powder diffraction

The main peaks in both XRPD and NPD data are consistent with a primitive, orthorhombic structure with unit cell $a \sim b \sim a_t\sqrt{2} \sim 5.4$ Å and $c \sim 23.7$ Å (t refers to a hypothetical tetragonal aristotype structure of $I4/mmm$ symmetry). The data could be fitted well with the reported noncentrosymmetric structure of $Pna2_1$ symmetry [11,12,38] (see [37]), although the polar displacement along the c axis is very small, and other possible structures (as described in Sec. III A) were also considered (see [37]).

The ISODISTORT software [32] was used to consider possible distortions, and the "mode inclusion method" [41,42] was employed, using the highest resolution backscattered (169°) NPD data, to determine which distortions gave the greatest improvement in fit. This analysis indicated that in-plane antipolar displacements (M_5^+) and in-plane axis octahedral tilts $a^-a^-c^0$ (X_3^-) gave significant improvements in fit, together lowering the symmetry to $Pnab$. [As discussed above, these two distortions couple and also allow the out-of-plane axis octahedral $a^0a^0c^-$ rotation (X_1^-).] Allowing further distortions, such as the out-of-plane polar displacement (Γ_3^-), to give the reported $Pna2_1$ model did not give a significant improvement in fit. Other similar models, including the $Pcaa$ model described above, as well as models of $Pcab$, $Pnaa$, and $P2_1ab$ symmetry, were also considered and could be discounted (see [37]).

A careful check was made for visible improvements in fit when moving from the nonpolar $Pnab$ model to either the polar $Pca2_1$ or $Pna2_1$ model, and although additional reflections are allowed for both polar models, no intensity was observed in these reflection positions (see [37]). Fitting statistics suggest a slight improvement in fit for the polar $Pna2_1$ model compared with the fit for the $Pnab$ model [R_{wp}'s of 4.09% (134 parameters) and 4.13% (109) parameters for the $Pna2_1$ and $Pnab$ models, respectively]. Hamilton t tests [43] were carried out using the fitting statistics for the highest resolution backscattered (169°) NPD data, and they suggested that the improvement in fit, given the increased number of parameters, is significant at the 25% significance level (an R factor ratio of 1.05 was obtained for comparison with the polar $Pna2_1$ model with the $Pnab$ model, compared with a calculated value of 1.01). However, this weighted residual method is known to be less reliable for differentiating between centrosymmetric and related noncentrosymmetric models for powder diffraction data [44], and in the absence of any visible improvement in fit (or conclusive physical property measurements consistent with a polar phase; see below), the centrosymmetric $Pnab$ model is the most appropriate to describe the average crystal structure of $Bi_2W_2O_9$. Final refinement details and selected bond lengths are given in Tables I and II, and refinement profiles are shown in Fig. 4(a). The structure is equivalent to what is illustrated in Fig. 1.

These diffraction data can only reveal the average, long-range crystal structure adopted by $Bi_2W_2O_9$; we note that bond valence sum calculations [45,46] give observed valences close to those expected for Bi^{3+} sites, but that W^{6+} sites are slightly overbonded (6.2–6.3) and we cannot rule out the possibility of short-range distortions (either polar or nonpolar) that might relieve this overbonding at a more local level.

TABLE I. Details from Rietveld refinement using room-temperature XRPD and NPD data for $Bi_2W_2O_9$ using the $Pnab$ model with $a = 5.433\,49(7)$ Å, $b = 5.413\,26(7)$ Å, $c = 23.6902(3)$ Å; $R_{wp} = 3.41\%$, $R_p = 6.93\%$, $\chi^2 = 5.37$ (109 parameters).

Atom	site	x	y	z	U_{iso} (Å^2)
Bi	8d	0.85422(9)	0.7298(1)	0.69600(2)	0.36(1)
W	8d	0.6657(1)	0.7449(2)	0.07670(3)	0.10(1)
O(1)	8d	−0.0752(1)	0.5099(1)	0.25004(4)	0.32(1)
O(2)	4c	0.25	0.3055(2)	0	0.48(2)
O(3)	8d	0.0808(1)	0.4534(1)	0.56642(3)	0.64(2)
O(4)	8d	0.5030(1)	0.0362(1)	0.58779(3)	0.53(1)
O(5)	8d	0.7243(1)	0.8131(1)	0.15224(4)	0.56(2)

C. SHG and dielectric polarization measurements

Second-harmonic-generation (SHG) measurements using 1064 nm radiation gave a low (0.2 times that of KDP) phase-matchable signal, suggesting a noncentrosymmetric component to the sample (see [37]). However, the threshold for laser damage of $Bi_2W_2O_9$ is low [the sample was visibly damaged by the laser with the off-white sample developing dark brown spots (see [37])]. Such laser damage has been shown to generate white light, including a green component, which could account for the low signal detected in these SHG measurements [47]. The results of these SHG measurements are therefore inconclusive as the SHG signal could arise from noncentrosymmetric decomposition products such as Bi_2WO_6 [48] or simply from optical breakdown of the material [47].

Dielectric polarization measurements were also carried out on sintered pellets of $Bi_2W_2O_9$. Care was taken not to introduce ferroelectric impurity phases during the sintering process, as noted in earlier studies [49]. Polarization versus electric field measurements carried out at a range of temperatures did not show any saturation in polarization (and no peaks in current density were observed) (Fig. 5), and they indicate that $Bi_2W_2O_9$ becomes increasingly leaky upon warming, in contrast to what was observed in ferroelectric Bi_2WO_6 (see [37]). Applying very large fields up to ± 250 kV cm^{-1} across the pellet at −40 °C did not reveal any field-dependent

TABLE II. Selected bond lengths from Rietveld refinement using room-temperature XRPD and NPD data for $Bi_2W_2O_9$ using the $Pnab$ model. Bond valence sum calculations suggest observed valences of 2.9 and 6.2 for Bi and W sites, respectively.

Bond	Length (Å)	Bond	Length (Å)
Bi—O(1)	2.1816(9)	W—O(2)	1.8936(7)
Bi—O(1)	2.2506(9)	W—O(3)	1.769(1)
Bi—O(1)	2.3131(9)	W—O(3)	2.150(1)
Bi—O(1)	2.4974(9)	W—O(4)	1.796(1)
Bi—O(5)	2.5192(9)	W—O(4)	2.141(1)
Bi—O(5)	2.5244(8)	W—O(5)	1.855(1)

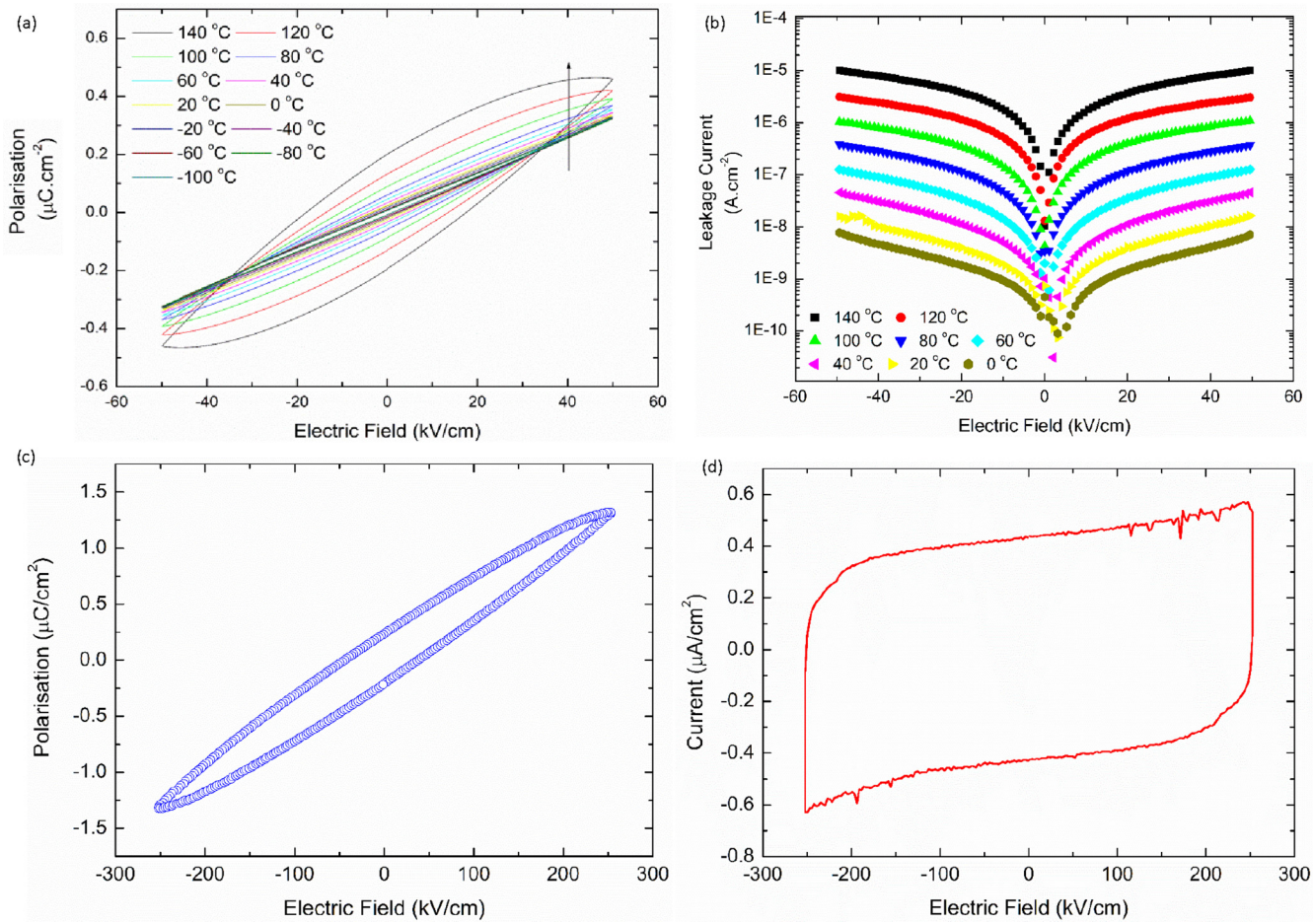

FIG. 5. Dielectric measurements on sintered pellets of $Bi_2W_2O_9$, (a) showing polarization and (b) showing leakage current with applied field at various temperatures; (c) and (d) show polarization and current density for fields up to ± 250 kV cm^{-1} at -40 °C.

behavior, and higher electric fields led to a dielectric breakdown of the material. So, although not confirming the antiferroelectric behavior, these dielectric measurements give no evidence for ferroelectricity in $Bi_2W_2O_9$ and are consistent with the assignment of the nonpolar, centrosymmetric *Pnab* symmetry at room temperature, as suggested above by first-principles calculations and NPD analysis.

IV. DISCUSSION

The diffraction data are consistent with the *Pnab* symmetry predicted from first-principles calculations, and, as illustrated in Fig. 4(b), refinements at room temperature also yield an atomic structure and amplitudes of distortions in good quantitative agreement with the computations. Moreover, the variable temperature XRPD data show a smooth decrease in unit-cell volume upon cooling (see [37]), with no evidence for discontinuities in lattice parameters that might indicate a low-temperature phase transition to another phase (although additional low-temperature NPD data would be necessary to confirm this), supporting the prediction that this model of *Pnab* symmetry is the ground state. Our structural model is also consistent with that described by Bando *et al.* in term of antipolar displacements of W^{6+} ions toward edges of the octahedra and a combination of tilts $a^-a^-c^-$ [12], but it suggests that the assignment of the polar $Pna2_1$ space group [11] is not correct. We find no evidence (from theory or experiment) for polarization along [001], and this is consistent with recent single-crystal x-ray diffraction experiments [56].

It is worth noting that the polar $A2_1am$ phase ($a^-a^-c^+$ tilts, with in-plane polar displacements) stated as the ground state of several other $n = 2$ Aurivillius phases (e.g., $Bi_2ANb_2O_9$, A = Sr,Ca,Ba,Pb [50]) has not been observed for $Bi_2W_2O_9$, but our calculations reveal that it is nevertheless a metastable phase with an energy only slightly above that of the nonpolar *Pnab* ground state.

Bando *et al.* first suggested the possibility of antiferroelectricity in $Bi_2W_2O_9$ [12]. Antiferroelectricity is not a property intrinsic to a specific structure, but it relates to the experimental ability to switch from a nonpolar (antipolar) ground state to a polar phase under an applied electric field, opening up a double-hysteresis P versus E loop [51]. This was recently reinvestigated by Rabe [13], who proposed practical conditions for a material to realize such a requirement: antiferroelectrics should show a ground state arising from a nonpolar distortion of a high-symmetry reference phase, and at the same time they should possess an alternative polar phase, appearing as a distortion of the same reference phase and sufficiently close in energy that an electric field can induce a first-order transition from the nonpolar ground state to that

polar phase. Guennou and Toledano [52] then built upon this to clarify the symmetry requirements for antiferroelectricity [52].

The *Pnab* and $A2_1am$ phases of $Bi_2W_2O_9$ satisfy the symmetry requirements of Guennou and Toledano [37], and from the calculations they appear sufficiently close in energy for a predicted electric field of ≈ 200 kV/cm to stabilize the polar phase over the ground state. Unfortunately, experimental measurements in fields up to 250 kV/cm were not able to realize this transition. This may result from materials science issues (e.g., microstructure considerations). It may also reflect the fact that the theoretical estimation of the switching field is too small or that the energy barrier between the two phases is large. This aspect warrants further investigation; in particular, strain engineering in thin films might tune the energy landscape and decrease the energy difference between the two phases, eventually inverting the relative stability of the two phases.

$Bi_2W_2O_9$ exhibits many similarities with WO_3, which was also recently proposed to be potentially antiferroelectric [34], and it is worth noting that the energy landscapes of both compounds share very similar features: the strongest instability is polar and produces, together with the antipolar instability, a more substantial gain in energy than octahedral rotations. However, the combination of antipolar motions and octahedral rotations yields a slightly larger gain in energy than polar motions, yielding a nonpolar ground state. The ground state of WO_3 involves a combination of antipolar distortions and octahedral rotations (the $P2_1/c$ symmetry model allowing $a^-a^-c^-$ rotations and antipolar displacement [34]) that is rather analogous to the pattern of displacements of the WO_3 bilayer in the *Pnab* phase of $Bi_2W_2O_9$. However, we note that (i) the antipolar displacement in WO_3 is different from those of $Bi_2W_2O_9$, i.e., the antipolar motion of W atoms in WO_3 is between [001] columns [inside one column the displacement is polar (see [37])] while the antipolar motion of W atoms in $Bi_2W_2O_9$ is between $[110]_t$ layers (inside one layer the displacement is polar); (ii) in bulk WO_3, combinations of antipolar distortions with either $a^-a^-c^-$ or $a^-a^-c^+$ give models of very similar energies in contrast to $Bi_2W_2O_9$, which gives models of very distinctive energies (see *Pnma* and *Pcca* or *Pnab* in Fig. 3).

Aurivillius phases are analogous in term of symmetry to Ruddlesden-Popper compounds, which are of potential interest as hybrid-improper ferroelectrics. It is interesting to compare $Bi_2W_2O_9$ with recently characterized $Sr_3Zr_2O_7$ and $Sr_3Sn_2O_7$ [53,54]. Both have polar $A2_1am$ ($a^-a^-c^+$) and nonpolar *Pnab* ($a^-a^-c^-$) states very close in energy, but in these $n = 2$ Ruddlesden-Popper phases, it is the polar $A2_1am$ phase that is the ground state. Both phases undergo first-order phase transitions to *Pnab* phases upon warming. However, these Sr-containing Ruddlesden-Popper phases differ from $Bi_2W_2O_9$ in that the energy gains from octahedral tilts (e.g., X_1^-, X_3^-, X_2^+) are much greater than those from polar or antipolar displacements ($\Gamma 5^-$ or $M5^+$), while for $Bi_2W_2O_9$ these latter distortions are at least twice as favorable as octahedral tilts. This illustrates that the appearance of the polarization in the $A2_1am$ is more "proper" in $Bi_2W_2O_9$ and "hybrid-improper" in the Ruddlesden-Popper phases [1]. This suggests that although *Pnab* and $A2_1am$ phases are close in energy, accessing the polar $A2_1am$ phase from the *Pnab* ground state and realizing antiferroelectric properties might require overcoming a significant energy barrier: this barrier might be due to not only "unwinding" the X_1^- ($a^0a^0c^-$) tilts (analogous to the loss of the $[001]_t$ tilt in the low-temperature–intermediate-temperature phase transition in Bi_2WO_6 [55]), but also removing the antipolar M_5^+ displacements to give the possible intermediate $a^-a^-c^0$ phase of *Cmcm* symmetry, which is high in energy. By contrast, this hypothetical intermediate *Cmcm* $a^-a^-c^0$ phase is relatively much lower in energy for both $Sr_3Zr_2O_7$ and $Sr_3Sn_2O_7$ [53,54]. It would be interesting to explore the effect of substitution of spherical cations such as La^{3+} into the bismuth sites in the fluorite-like layers (while maintaining the Aurivillius structure) to see how the balance of energies of the Γ_5^- or M_5^+ displacements and octahedral tilts can be tuned.

V. CONCLUSIONS

We have shown consistently from first-principles simulations and experimental work that the ground state of the $n = 2$ Aurivillius $Bi_2W_2O_9$ structure is a nonpolar phase of *Pnab* symmetry. This phase appears as a small distortion of the paraelectric $I4/mmm$ parent phase involving an in-plane antipolar displacement of W and Bi cations and in-plane and out-of-plane octahedral tilts ($a^-a^-c^-$). Close in energy to this ground state, we identified a metastable polar phase of $A2_1am$ symmetry, involving an in-plane polar displacement of W and Bi cations and in-plane and out-of-plane octahedral tilts ($a^-a^-c^+$). The energy proximity between these polar and antipolar phases, related by a first-order phase transition, makes $Bi_2W_2O_9$ a potential antiferroelectric material. The electric field required to stabilize the $A2_1am$ phase against the *Pnab* ground state was estimated theoretically to be 190 kV cm^{-1}. Experimentally, we confirm the nonferroelectric character of $Bi_2W_2O_9$, but applying fields up to ± 250 kV cm^{-1} was not sufficient to reveal the antiferroelectric behavior. This should, however, be investigated by applying larger fields. The antiferroelectric character might also be favored and revealed by appropriate strain engineering of the energy landscape.

Note added. During preparation of this manuscript, we became aware of the single-crystal x-ray diffraction study on $Bi_2W_2O_9$, which also proposes a ground state of *Pnab* symmetry [56] fully consistent with our work.

ACKNOWLEDGMENTS

Computational resources are provided by the Consortium des Equipements de Calcul Intensif (CECI), funded by the F.R.S.-FNRS under Grant No. 2.5020.11 and the Tier-1 supercomputer of the Fédération Wallonie-Bruxelles funded by the Walloon Region under Grant No 1117545. H.D. and Ph.G. acknowledge support from Algerian-WBI bilateral cooperative project. We are grateful to the ISIS Neutron and Muon Source for provision of NPD time through the HRPDXpress scheme [57] and to A. Gibbs and D. Fortes for their assistance. E.B. and E.E.M. are grateful to the Royal Society (IES-R3-170112) and to the Leverhulme Trust (RPG-2017-362) for funding. W.Z. and P.S.H. thank the Welch Foundation (Grant No. E-1457) for support.

[1] N. A. Benedek, J. M. Rondinelli, H. Djani, P. Ghosez, and P. Lightfoot, Dalton Trans. **44**, 10543 (2015).

[2] N. A. Benedek and C. J. Fennie, Phys. Rev. Lett. **106**, 107204 (2011).

[3] N. A. Benedek, Inorg. Chem. **53**, 3769 (2014).

[4] C. H. Hervoches and P. Lightfoot, Chem. Mater. **11**, 3359 (1999).

[5] N. C. Hyatt, I. M. Reaney, and K. S. Knight, Phys. Rev. B **71**, 024119 (2005).

[6] H. Djani, E. Bousquet, A. Kellou, and P. Ghosez, Phys. Rev. B **86**, 054107 (2012).

[7] R. L. Withers, J. G. Thompson, and A. D. Rae, J. Solid State Chem. **94**, 404 (1991).

[8] J. M. Perez-Mato, M. Aroyo, A. García, P. Blaha, K. Schwarz, J. Schweifer, and K. Parlinski, Phys. Rev. B **70**, 214111 (2004).

[9] J. M. Perez-Mato, P. Blaha, K. Schwarz, M. Aroyo, D. Orobengoa, I. Etxebarria, and A. García, Phys. Rev. B **77**, 184104 (2008).

[10] H. Okudera, Y. Sakai, K. Yamagata, and H. Takeda, Acta. Cryst. B **74**, 295 (2018).

[11] J.-C. Champarnaud-Mesjard, B. Frit, and A. Watanabe, J. Mater. Chem. **9**, 1319 (1999).

[12] Y. Bando, A. Watanabe, Y. Sekikawa, M. Goto, and S. Horiuchi, Acta Cryst. Sect. A **35**, 142 (1979).

[13] K. M. Rabe, Antiferroelectricity in oxides: A reexamination, in *Functional Metal Oxides* (Wiley, 2013), Chap. 7, pp. 221–244.

[14] P. Boullay, J. Tellier, D. Mercurio, M. Manier, F. J. Zuñiga, and J. M. Perez-Mato, Solid State Sci. **14**, 1367 (2012).

[15] R. Machado, M. G. Stachiotti, R. L. Migoni, and A. H. Tera, Phys. Rev. B **70**, 214112 (2004).

[16] P. Hohenberg and W. Kohn, Phys. Rev. **136**, B864 (1964).

[17] W. Kohn and L. J. Sham, Phys. Rev. **140**, A1133 (1965).

[18] X. Gonze, J.-M. Beuken, R. Caracas, F. Detraux, M. Fuchs, G.-M. Rignanese, L. Sindic, M. Verstraete, G. Zerah, F. Jollet, M. Torrent, A. Roy, M. Mikami, P. Ghosez, J.-Y. Raty, and D. Allan, Comput. Mater. Sci. **25**, 478 (2002).

[19] X. Gonze, G. M. Rignanese, M. Verstraete, J. M. Beuken, Y. Pouillon, R. Caracas, F. Jollet, M. Torrent, G. Zerah, M. Mikami, P. Ghosez, M. Veithen, J. Y. Raty, V. Olevano, F. Bruneval, L. Reining, R. Godby, G. Onida, D. R. Hamann, and D. C. Allan, Z. Kristallogr. **220**, 558 (2005).

[20] X. Gonze, B. Amadon, P.-M. Anglade, J.-M. Beuken, F. Bottin, P. Boulanger, F. Bruneval, D. Caliste, R. Caracas, M. Côté, T. Deutsch, L. Genovese, P. Ghosez, M. Giantomassi, S. Goedecker, D. Hamann, P. Hermet, F. Jollet, G. Jomard, S. Leroux, M. Mancini, S. Mazevet, M. Oliveira, G. Onida, Y. Pouillon, T. Rangel, G.-M. Rignanese, D. Sangalli, R. Shaltaf, M. Torrent, M. Verstraete, G. Zerah, and J. Zwanziger, Comput. Phys. Commun. **180**, 2582 (2009).

[21] J. P. Perdew, A. Ruzsinszky, G. I. Csonka, O. A. Vydrov, G. E. Scuseria, L. A. Constantin, X. Zhou, and K. Burke, Phys. Rev. Lett. **100**, 136406 (2008).

[22] M. van Setten, M. Giantomassi, E. Bousquet, M. Verstraete, D. Hamann, X. Gonze, and G.-M. Rignanese, Comput. Phys. Commun. **226**, 39 (2018).

[23] H. Monkhorst and J. Pack, Phys. Rev. B **13**, 5188 (1976).

[24] H. B. Schlegel, J. Comput. Chem. **3**, 214 (1982).

[25] S. Baroni, S. de Gironcoli, A. Dal Corso, and P. Giannozzi, Rev. Mod. Phys. **73**, 515 (2001).

[26] X. Gonze and C. Lee, Phys. Rev. B **55**, 10355 (1997).

[27] R. Resta, Rev. Mod. Phys. **66**, 899 (1994).

[28] H. M. Rietveld, J. Appl. Cryst. **2**, 65 (1969).

[29] A. A. Coelho, J. Appl. Cryst. **36**, 86 (2003).

[30] A. March, Z. Kristallogr. Cryst. Mater. **81**, 285 (1932).

[31] W. A. Dollase, J. Appl. Cryst. **19**, 267 (1986).

[32] B. J. Campbell, H. T. Stokes, D. E. Tanner, and D. M. Hatch, J. Appl. Cryst. **39**, 607 (2006).

[33] K. M. Ok, E. O. Chi, and P. S. Halasyamani, Chem. Soc. Rev. **35**, 710 (2006).

[34] H. Hamdi, E. K. H. Salje, P. Ghosez, and E. Bousquet, Phys. Rev. B **94**, 245124 (2016).

[35] R. Zhang, M. Senn, and M. A. Hayward, Chem. Mater. **28**, 8399 (2016).

[36] When distinct modes j of a given symmetry contribute to the same distortion Δ, their total contribution corresponds to $A\sqrt{(\sum_j \alpha_j^2)}$.

[37] See Supplemental Material at http://link.aps.org/supplemental/10.1103/PhysRevB.101.134113 for refinement details for $Pna2_1$ and $Pca2_1$ models, analysis of variable temperature XRPD data for $Bi_2W_2O_9$, SHG tests and dielectric measurements for $Bi_2W_2O_9$ and Bi_2WO_6, comments on criteria for antiferroelectricity, details of the relative contribution of the different modes involved in the distortions and the schematic antipolar displacement in WO_3.

[38] M. Mackza, L. Macalik, and J. Hanuza, J. Raman Spectrosc. **40**, 2099 (2009).

[39] R. Resta, M. Posternak, and A. Baldereschi, Phys. Rev. Lett. **70**, 1010 (1993).

[40] The computed value of the polarization is at 0 K but typically a good estimate of the experimental value, far enough from the transition temperature.

[41] A. J. Tuxworth, E. E. McCabe, D. G. Free, S. J. Clark, and J. S. O. Evans, Inorg. Chem. **52**, 2078 (2013).

[42] E. E. McCabe, C. Stock, E. E. Rodriguez, A. S. Wills, J. W. Taylor, and J. S. O. Evans, Phys. Rev. B **89**, 100402(R) (2014).

[43] W. C. Hamilton, Acta Cryst. **18**, 502 (1965).

[44] J. W. Whitaker and A. Jeffery, Acta Cryst. **23**, 984 (1967).

[45] I. D. Brown and D. Altermatt, Acta Cryst. B **41**, 244 (1985).

[46] N. E. Brese and M. O'Keefe, Acta Cryst. B **47**, 192 (1991).

[47] Bandis, L. Cramer, T. E. Holt, S. C. Langford, and J. T. Dickinson, Appl. Surf. Sci. **197-198**, 100 (2002).

[48] K. S. Knight, Min. Mag. **56**, 399 (1992).

[49] D. C. Feteira and A. Sinclair, J. Am. Ceram. Soc. **91**, 1338 (2008).

[50] S. M. Blake, M. J. Falconer, M. McCreedy, and P. Lightfoot, J. Mater. Chem. **7**, 1609 (1997).

[51] M. E. Lines and A. M. Glass, *Principles and Applications of Ferroelectrics and Related Materials* (Oxford University Press, 2001).

[52] P. Toledano and M. Guennou, Phys. Rev. B **94**, 014107 (2016).

[53] S. Yoshida, K. Fujita, H. Akamatsu, O. Hernandez, A. S. Gupta, F. G. Brown, H. Padmanabhan, A. S. Gibbs, T. Kuge, R. Tsuji, S. Murai, J. M. Rondinelli, V. Gopalan, and K. Tanaka, Adv. Funct. Mater. **28**, 1801856 (2018).

[54] S. Yoshida, H. Akamatsu, R. Tsuji, O. Hernandez, H. Padmanabhan, A. S. Gupta, A. S. Gibbs, K. Mibu, S. Murai, J. M. Rondinelli, V. Gopalan, K. Tanaka, and K. Fujita, J. Am. Chem. Soc. **140**, 15690 (2018).

[55] N. A. McDowell, K. S. Knight, and P. Lightfoot, Chem. Eur. J. **12**, 1493 (2006).

[56] X. Tian, Z. Gao, F. Chen, Q. Wu, C. Li, W. Lu, Y. Sun, and X. Tao, CrystEngComm **20**, 2669 (2018).

[57] DOI: 10.5286/ISIS.E.RB1790213-1.